PAPER

Check for updates

Water-assisted synthesis of stable and multicolored CsPbX₃@SiO₂ core–shell nanoparticles as fluorescent probes for biosensing†

Cynthia Collantes, [ID] [a] William Teixeira, [ID] [a] Victoria González-Pedro, [ID] *[a,b] María-José Bañuls, [ID] [a,b] Pedro Quintero-Campos, [ID] [a] Sergi Morais [ID] [a,b,c] and Ángel Maquieira[a,b,c]

Colloidal lead halide perovskite nanocrystals are highly luminescent materials with great promise as fluorescent probes in biosensing as long as their intrinsic instability in aqueous media is effectively addressed. In this study, we successfully prepared stable and multicolored CsPbX₃@SiO₂ (X = Cl/Br, Br and I) core–shell nanoparticles through a simple method based on the water-induced transformation of Cs₄PbX₆ into CsPbX₃, combined with sol–gel procedures. We observed that the concentration of the Cs₄PbX₆ precursor plays a crucial role in the formation of isolated nanospheres with uniform silica coating and in controlling the number of core-free particles. Furthermore, our research expands this approach to other halide compositions, resulting in multicolored core–shell nanoparticles with emission wavelengths ranging from 490 to 700 nm, average sizes below 30 nm, and photoluminescence quantum yields close to 60%. Unlike in previous reports, the silica coating boosts the photoluminescence quantum yields compared to uncoated counterparts and provides increased structural stability for more than four days. Moreover, a controlled thermal treatment confers water stability to the as-synthesized nanoparticles. To establish the feasibility of the developed materials as fluorescent probes, we successfully demonstrated their specific recognition of a humanized antibody (omalizumab) used in treating patients with severe allergic asthma. This work paves the way to develop *in vitro* tests using CsPbX₃@SiO₂ core–shell nanoparticles as fluorogenic probes.

1.   Introduction

Colloidal nanocrystals (NCs) of CsPbX₃ metal halide perovskites (MHPs) have garnered significant attention in multiphoton-imaging applications and lighting materials. These NCs possess remarkable properties, including an ultrahigh photoluminescence (PL) quantum yield (∼99%),[1] tunable emission properties with a wide color gamut,[2] and unprecedented multi-photon absorption cross-sections.[3] Moreover, their ease

[a]Instituto Interuniversitario de Investigación de Reconocimiento Molecular y Desarrollo Tecnológico (IDM), Universitat Politècnica de València-Universitat de València, Camino de Vera s/n, E46022 València, Spain.
E-mail: vigonpe@upvnet.upv.es
[b]Departamento de Química, Universitat Politècnica de València, Camino de Vera s/n, E46022 València, Spain
[c]Unidad Mixta UPV-La Fe, Nanomedicine and Sensors, IIS La Fe, Valencia, Spain

of synthesis and cost-effectiveness further contribute to their appeal.[4] As a result, these NCs have emerged as promising luminescent tags for imaging, biosensing, and clinical diagnosis. However, two main challenges need to be addressed to establish their viability as luminescent probes. First, the synthesis of water-stable NPs is essential to ensure their stability and functionality in aqueous media. Second, it is crucial to fabricate nano-sized monodisperse particles that remain structurally intact under various chemical environments and processing conditions, enabling precise biomolecule conjugation at a single particle level.[5,6]

To overcome this matter, the surface of the NCs needs to be protected with materials that chemically prevent water from reaching the NC surface. A wide range of materials including metal oxides, polymers, MOFs, metal chalcogenides, and perovskite derivatives have been used as shells to protect the surface of perovskite NCs.[7] Among various encapsulants, SiO₂ has received significant interest because of its transparency, biocompatibility, and chemical stability. However, coating SiO₂ shells on MHP NCs is challenging because the hydrolysis reaction requires some amount of water that degrades the NCs.

Several attempts have been made to coat SiO_2 on MHP NCs to reduce or eliminate the amount of water, yielding multiple NC-embedded SiO_2 matrices.[8–16] Another approach that is often used is the *in situ* crystallization of perovskite NCs inside mesoporous silica nanoparticles by intercalating salt precursors and thermal treatment. The studies showed that mesoporous encapsulation enhances the stability of MHPs and prevents halide ion exchange when NCs of two different halides are mixed.[17,18]

In an alternative promising strategy for encapsulating metal halide perovskites, several research groups have exploited the transformative properties of metal halides, specifically the 0D Cs_4PbBr_6 into 3D $CsPbBr_3$ transformation features to synthesize core–shell nanoparticles and nanocomposites. This transformation can be achieved by creating a Pb-enriched environment[19] or a Cs-deficient situation where the $CsPbX_3$ phase is more stable. For example, in the nonpolar-water interphase, CsX ions are stripped from the Cs_4PbX_6 due to their ionic nature and high solubility in water,[20] resulting in luminescent $CsPbBr_3$ NCs. Other approaches involve the use of Cs^+-adsorbent materials such as Prussian blue[21] and thermal annealing as a physical strategy to induce phase conversion.[22] In addition to these approaches, Udayabhaskararao *et al.* described spontaneous transformation from $CsPbX_3$ into Cs_4PbX_6 NCs (and *vice versa*) by adjusting the oleylamine : oleic acid ratio.[23] Recently, Baranov *et al.* reported that poly(maleic anhydride-1-*alt*-octadecene) (PMAO) triggered phase transformation[24] where the polymer destabilizes the Cs_4PbX_6 NC surface by the removal of olefin ligands, inducing the formation of $CsPbBr_3$ NCs.

The route of transformation from 0D into 3D results in the production of $CsPbBr_3$ NCs that exhibit improved stability in polar media.[20] This issue presents an opportunity to apply the systematic sol–gel process to grow a silica (SiO_2) shell on the NC surface, thereby enhancing their stability towards moisture. Some studies have successfully combined transformation-triggering conditions with a sol–gel process. For instance, Hu *et al.* encapsulated $CsPbX_3$ (X = Cl/Br, Br, Br/I and I) into a Janus-type SiO_2 heterostructure of 18 nm with a PLQY of 80%. To obtain entirely coated NPs, Li *et al.* incorporated a pre-silanization step of Cs_4PbBr_6 NCs with partially hydrolyzed TMOS (PH-TMOS).[25] This method introduces silanization seeds on the MHP NC surface before phase conversion and encapsulation, giving $CsPbBr_3@SiO_2$ core–shell NPs of 60 nm with a PLQY of 65%. In an alternative approach, Park *et al.* used nitric acid to accelerate the hydrolysis of tetraethyl orthosilicate (TEOS).[26] However, instead of obtaining isolated colloidal NPs, they obtained composites. In this research line, Rossi *et al.* exploited a transformation route triggered by maleic anhydride, synthesizing $CsPbBr_3@SiO_2$ NPs of 22–33 nm with a PLQY of 1–4%.[27]

In this study, we have successfully synthesized multicolored $CsPbX_3@SiO_2$ (X = Cl/Br, Br and I) core–shell NPs with remarkable and tunable emission wavelengths, which offer excellent potential as a multimodal fluorescent tag for imaging and biosensing, in health or biotechnological applications. Our work is based on the water-triggered phase transformation of 0D Cs_4PbBr_6 NCs into $CsPbBr_3$ NCs in the presence of TMOS. Moreover, long-term stable and water-dispersible perovskite NPs were also obtained under a controlled thermal treatment. Finally, to demonstrate the suitability of these materials as fluorescent labels, as-synthesized NPs were conjugated to a humanized antibody, and the specific recognition of its paratope was proved in a direct immunoassay as a proof of concept.

2. Experimental section

2.1. Materials

Cesium carbonate (Cs_2CO_3, 99.9%, Sigma Aldrich), lead bromide ($PbBr_2$, ≥98%, Sigma Aldrich), lead iodide (PbI_2, 98.5%, Alfa Aesar), lead chloride ($PbCl_2$, 99%, Alfa Aesar), 1-octadecene (ODE, 90% tech, Sigma Aldrich), oleic acid (OA, tech. 90%, Alfa Aesar), oleylamine (OAm, approximate C18-content 80–90%, Sigma Aldrich), tetramethyl orthosilicate (TMOS, 99%, ACROS Organics), toluene and hexane.

2.2. Synthesis of Cs_4PbX_6 NCs (X = Br, I and mixed composition of Cl/Br)

Cs_4PbX_6 NCs were prepared *via* the hot-injection method described by Akkerman with some modifications.[19] Briefly, a 100 mL 3-neck flask containing 0.2 mmol PbX_2 (0.1 mmol of each lead halide for the mixed composition), 5 mL of ODE and 0.2 mL of OA was heated under mild stirring and vacuum at 120 °C for 30 min. Then, 1.5 mL of OAm was injected under an inert atmosphere until the solution became clear, indicating that PbX_2 was entirely dissolved, and the flask was cooled down to room temperature.

The flask was heated again under vacuum and mild stirring to reach the optimal temperature (60 °C for PbI_2, 80 °C for $PbBr_2$, and 100 °C for the mixture $PbCl_2$ + $PbBr_2$), and it was left for 15 more min. After an injection of 0.5 mL of Cs–OA (400 mg of Cs_2CO_3 previously dissolved in 8 mL of OA under vacuum at 100 °C), the solution turned turbid within 15–30 s, and finally, the flask was cooled down to room temperature. The total volume was distributed into four microtubes and centrifuged at 4000 rpm for 5 min. The sediment was dispersed in ~5 mL of anhydrous hexane. The concentration of the stock solution was determined by weighing mass residues after solvent removal during the purification step: 25.74 ± 3.38 mg mL^{-1} for Cs_4PbBr_6, 35.19 ± 1.07 mg mL^{-1} for Cs_4PbI_6 and 28.75 ± 1.54 mg mL^{-1} for $Cs_4Pb(Cl_xBr_{6-x})$.

2.3. Synthesis of $CsPbX_3@SiO_2$ core–shells (X = Br, I and mixed composition of Cl/Br)

To prepare core–shell NPs, 2 μL of partially hydrolyzed TMOS (prepared by adding 2 mL of toluene, 12 μL of Milli-Q H_2O filtered with a 0.45 μm filter and 198 μL of TMOS into a glass vial and stirring at 500 rpm for 18 h) was added to 2 mL of a solution of Cs_4PbX_6 NCs. After stirring at 500 rpm for 5 h, 10 μL of TMOS was added under magnetic stirring at 900 rpm

for 1 min. Afterward, 300 μL of Milli-Q H_2O was added under magnetic stirring at 1200 rpm for 2 min. The vial remained undisturbed overnight. Core–shell NPs were purified by centrifugation at 9000 rpm for 5 min.

To obtain water-resistant core–shell NPs, 5 mL of the NCs@SiO$_2$ NPs was placed in a porcelain plate and calcined at 565 °C for 10 min with a mean heating rate of 1 °C min^{-1} in a muffle furnace under an air atmosphere. After cooling to room temperature, the sample was dispersed in water and ultrasonicated for 30 min before TEM preparation.

2.4. Immunoassay

(i) Preparation of core–shell NPs derivatized with amine groups (MHP@SiO$_2$–NH$_2$). 10.5 mg of CsPbX$_3$@SiO$_2$ NPs and 6 μL of (3-aminopropyl)triethoxysilane were added to 1 mL of anhydrous toluene and stirred for 5 h. Functionalized NPs were purified by centrifugation at 9000 rpm and resuspended first in ethanol and then in 3.75 mL of phosphate buffered saline. *(ii) Preparation of NP-αIgE perovskite–omalizumab conjugates.* 25 μL of omalizumab (humanized antibody used in asthma treatment) at 1.5 mg mL^{-1} was added to MHP@SiO$_2$–NH$_2$ NPs and incubated overnight at 4 °C. Conjugated NPs were centrifuged, and the resultant sediment was dispersed in 250 μL of 10 mM sodium phosphate buffer, 150 mM NaCl, and 0.05% Tween 20, pH 7 (PBS-T). *(iii) Direct immunoassay.* A black polystyrene 96-well plate was coated overnight at 4 °C with 5 mg L^{-1} of a specific paratope receptor (100 μL per well) in 50 mM sodium carbonate/bicarbonate buffer, pH 9.6. Ovalbumin was used (5 mg L^{-1}) as the negative control. The plate was washed four times with PBS-T. Then, 100 μL per well of the *NP-αIgE* conjugates were added and incubated for 1 h at room temperature. After washing the plate six times with PBS-T, PL spectra were measured using an EnSpire multimode plate reader (PerkinElmer).

2.5. Characterization methods

UV–vis absorption spectra were recorded using a UV–visible spectrophotometer (Agilent 8453, Agilent Technologies). The photoluminescence spectra were obtained using a spectrofluorometer (PTI QMA4, Horiba) at an excitation wavelength of 355 nm for all spectra. The PLQY was determined by using quinine sulfate in 0.5 M H_2SO_4 ($\Phi = 0.45$) as a standard for the CsPb(Cl$_x$Br$_{3-x}$) and CsPbBr$_3$ NPs at an excitation wavelength of

310 nm. TEM images were taken using a transmission electron microscope at 120 kV (JEM-1400, Flash) and a field emission transmission electron microscope at 200 kV equipped with an X-ray detector (JEM 2100F, JEOL).

3. Results and discussion

For the preparation of core–shell NPs, Cs$_4$PbX$_6$ NCs (X = Cl/Br, Br, and I) were synthesized according to the procedure described by Akkerman *et al.*[19] The synthesis yielded NPs that presented characteristic absorption peaks at 305, 314, and 367 nm (Fig. S1†) and exhibited hexagonal or rhombohedral morphology with mean particle sizes of 18.97 ± 2.84 nm, 14.83 ± 1.62 nm, and 17.59 ± 2.99 nm, respectively (Fig. S2†).

The Cs$_4$PbX$_6$ NCs were first silanized using partially hydrolyzed TMOS (PH TMOS). At this step, the silanol groups of TMOS, attached to the Cs$_4$PbX$_6$ NC surface, replaced the original hydrophobic olefin precursor and introduced growth sites for the condensation of the SiO$_2$ network. In the second step, silane-derivatized NCs were treated with a TMOS aqueous solution, which promoted the 0D to 3D phase transition *via* CsX stripping and shell formation around the transformed NCs *via* condensation of TMOS.[25] A schematic representation of the formation mechanism of core–shell NPs from Cs$_4$PbX$_6$ NCs is illustrated in Fig. 1.

To optimize the Cs$_4$PbX$_6$ NC concentration for the synthesis of CsPbX$_3$@SiO$_2$ NPs, serial dilutions were tested, starting from the following concentrations of the purified NCs: 14.4, 25.7 and 17.6 mg mL^{-1} for Cs$_4$Pb (Cl$_x$Br$_{6-x}$), Cs$_4$PbBr$_6$ and Cs$_4$PbI$_6$, respectively. Fig. S3† summarizes the transmission electron microscopy (TEM) results of three representative concentrations per composition, and Table S1† provides structural features of the resulting core–shell NPs.

It should be observed that, independent of the halide composition, high starting material concentrations produce a heterogeneous population of NPs, containing uncoated crystals of different sizes and shapes and silica spheres with or without a nanocrystal core. It may be associated with the more extensive formation of CsPbBr$_3$ NCs, which reduces the coating efficiency of the silane, leading to the evolution of the uncoated NPs into other perovskite structures.[28] At an intermediate concentration, uniform-sized monodisperse NPs are prevalent, while at low concentrations, the presence of core-
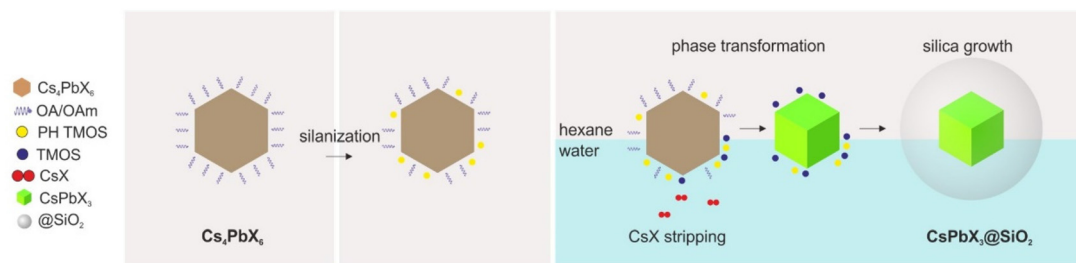

Fig. 1 Scheme of the core–shell NP formation mechanism.

free silica nanoparticles increases. It could be explained that decreasing CsPbBr$_3$ NCs would facilitate homogeneous nucleation, resulting in the prevalence of core-free NPs.

Fig. S3† shows how remarkable the reduction of the core size is when comparing the intermediate and the lowest concentrations (from 11 to 3 nm in CsPb(Cl$_x$Br$_{3-x}$)@SiO$_2$, from 4 to 2 nm in CsPbBr$_3$@SiO$_2$ and from 2 nm to almost undetectable or coreless nanospheres in CsPbI$_3$@SiO$_2$). This behavior is due to the increase in the water : Cs$_4$PbX$_6$ ratio, which shifts the equilibrium of the CsX stripping reaction (Cs$_4$PbBr$_6$ → CsPbBr$_3$ + 3CsX), producing smaller core particles.

Regarding the emission properties, the right panel of Fig. S3† shows the PL intensity and maximum wavelength for different tested serial dilutions. It must be noticed that the emission peak presents similar features for the intermediate and lower concentrations, while a slight blue shift is observed for the highest one. This shift could be attributed to the heterogeneous NP population obtained under the synthesis conditions.

With regard to the particle uniformity and PL emission intensity, we chose 7.2 mg mL^{-1}, 3.2 mg mL^{-1} and 2.2 mg mL^{-1} Cs$_4$PbX$_6$ (X = Cl/Br, Br and I) as the optimal concentrations for preparing CsPbX$_3$@SiO$_2$ NPs. Fig. 2 shows the absorption/emission spectra and TEM images of the resulting nanoparticles. Table 1 presents information about the emission peak, full width at half maximum (fwhm), PLQY, mean particle diameter, core size, and number of cores per particle, including NP features of the most representative works in the literature. From these data, it is noteworthy that all samples showed relatively sharp peaks with the full width at half-maximum in the 22 to 33 nm range. Our developed CsPbX$_3$@SiO$_2$ core–shell NPs presented the tiniest particle sizes reported in the literature by water-assisted synthesis methodologies while preserving the emission quantum yield. In addition, the methods described are extended to other halide compositions of NPs, obtaining multi-colored NPs with a color gamut from blue to red. Concerning the PLQY, coated NPs exhibited an enhancement of emission efficiency of 44%
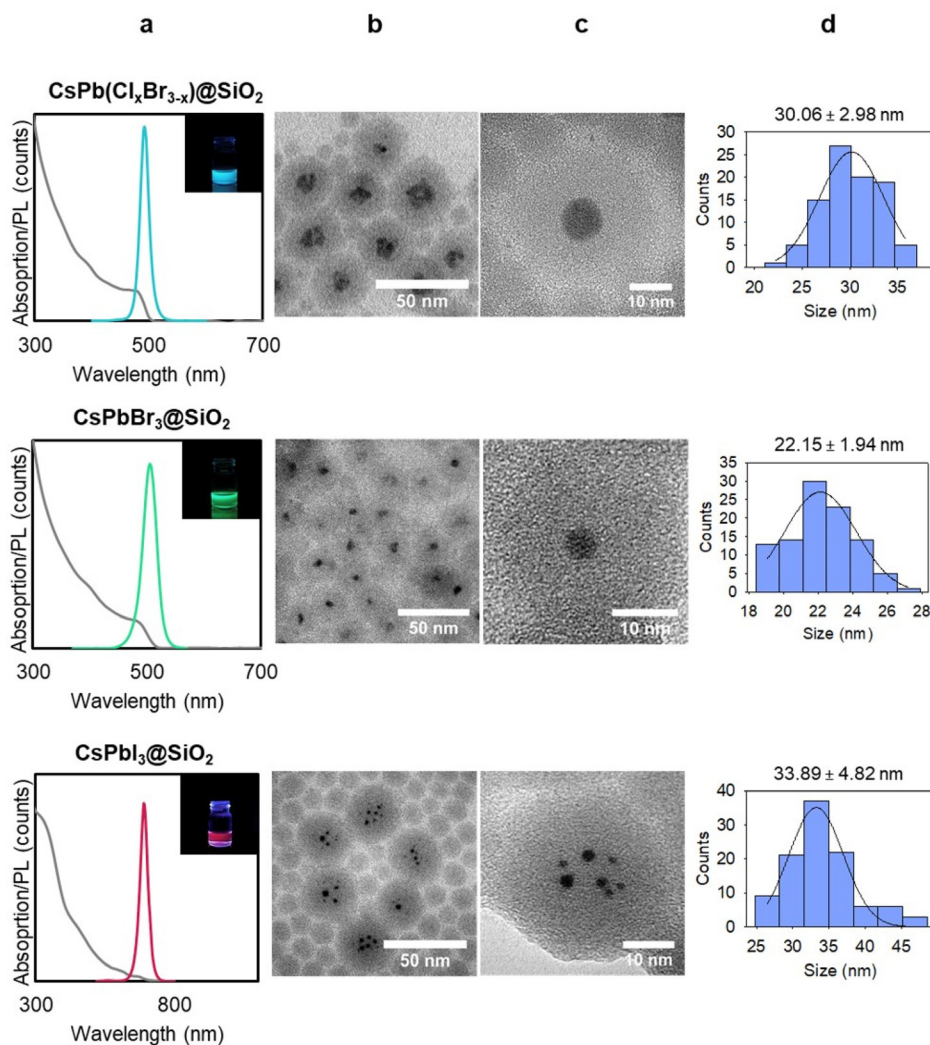

Fig. 2 Optical and structural characterization of the CsPbX$_3$@SiO$_2$ NPs. (a) UV−vis absorption and PL spectra recorded at an excitation wavelength of 355 nm, (b) low and (c) high magnification TEM images and (d) histogram showing the particle size distribution.

Table 1 Properties of the as-prepared CsPbX$_3$@SiO$_2$ NPs (X = Cl/Br, Br, and I) at the selected concentrations 7.2, 3.2 and 2.2 mg mL^{-1}, respectively

Composition	Emission peak (nm)	Fwhm (nm)	PLQY	Particle size (nm)	Core size (nm)	Cores/particle (nm)	Ref.
Cs$_4$PbBr$_6$ to CsPbBr$_3$ phase transition							
CsPb(Cl$_x$Br$_{3-x}$)@SiO$_2$	492	26	18%	30.06 ± 2.98	11.62 ± 2.1	1	This work
CsPbBr$_3$@SiO$_2$	506	22	57%	22.15 ± 1.94	4.26 ± 0.9	1	
CsPbI$_3$@SiO$_2$	689	33	N.R^a	33.89 ± 4.82	2.05 ± 0.46	5	
CsPbBr$_3$@SiO$_2$	521	16.4	65%	60	12.25	1	25
CsPbBr$_3$@SiO$_2$	507	20	8%	17	10	1	27
Ligand assisted reprecipitation							
CsPbBr$_3$@SiO$_2$	501	22	88	26	10.5	1	29
Hot injection							
CsPbBr$_3$@SiO$_2$	519	16	87	NR	NR	1	30

^{a} Not reported. The PLQY for CsPbI$_3$ was not determined due to the low sample stability.

and 32% regarding the uncoated CsPb(Cl$_x$Br$_{3-x}$) and CsPbBr$_3$ counterparts. These results highlight the beneficial role of silica in shallow defect passivation of CsPbX$_3$ NCs formed *via* the water-induced transformation of Cs$_4$PbX$_6$ NCs. It should be considered that, according to the literature, NPs of comparable sizes to ours are poor emitters.[27] Paying attention to our data, it is worth mentioning that we synthesized core–shell NPs that cover all the practical needs to be exploited as a fluorescent label for biosensing, such as tunable emission properties through the visible region, sharp emission peaks, and reduced particle size (20–30 nm). Although studies exist that describe core–shell NPs with significant PLQYs and within those sizes, they are devoted to Br compositions, do not report evidence on the formation of core–shell NPs of other halide compositions, and do not provide size dispersion analysis.[29–31]

The core dimensions' size-shrinkage of CsPbX$_3$ compared to their precursor NCs is explained by the CsX-stripping mechanism.[20,24,25,32] Cs$_4$PbX$_6$ NCs are CsX-rich perovskite structures; therefore, upon water treatment, stripping of CsX occurs because of the ionic nature of Cs$_4$PbX$_6$ and the very high solubility of CsX in water, which lead to the decomposition of Cs$_4$PbX$_6$ and the formation of CsPbX$_3$ NCs. During the process, the rhombohedral Cs$_4$PbX$_6$ NCs are converted into simple cubic structured CsPbX$_3$ NCs, and this could be confirmed by the shrinkage of the particle size.[20] In our work, the reported size reduction (32%, 75%, and 88% for X = Cl/Br, Br, and I) is more significant than the one described in the literature. This fact might be caused by the harsher conditions in our method, which ended up etching, to a greater extent, the 3D nanocrystal surface. On the other hand, there also appeared to exist a correlation between the halide nature and the size and number of cores per particle. We attributed this behavior to the relative extrinsic stability of ternary cesium halide perovskites towards water and the oxidant environment, which decreases in the order CsPbCl$_3$ > CsPbBr$_3$ > CsPbI$_3$. This behavior may be associated with substituting larger I, by Br or Cl, leading to the reduction of lattice constants and transition to the cubic phase, which is a more compact and stable structure than the tetragonal pseudo-cubic phase.[33,34] Hence, the

degradation of the as-formed NCs is accelerated in iodine species, leading to crystal decomposition, core size reduction before silica shell formation, and simultaneous encapsulation of several cores per particle.

Table S2 and Fig. S4† show the coexistence and ratio of core–shell to empty SiO$_2$ nanoparticles for each composition. The results are 29.1% in CsPbCl$_x$Br$_{3-x}$@SiO$_2$, 78.2% in CsPbBr$_3$@SiO$_2$, and 6.8% in CsPbI$_3$@SiO$_2$. The presence of core-free silica nanoparticles in the samples could be explained according to the LaMer theory,[35,36] which claims that to ensure coated perovskite NCs without core-free SiO$_2$ particles, the monomer concentration must fulfill the conditions of C < Chomo throughout the reaction process, where Chomo is the homogeneous nucleation TMOS concentration threshold. In our method to prevent perovskite degradation, the concentration of TMOS is large, thus core–shell and core-free nanoparticles co-exist in the final product. Future research is mandatory to achieve effective coating without core-free silica NPs as long as they lead to a loss of the effective fluorescence signal. This matter could be addressed by the following: (i) the fractionated drop method, which can always meet the above-mentioned conditions, in which fresh TMOS is added after the previous TMOS is consumed,[37] and (ii) replacing TMOS with TEOS, which presents slower condensation rates, thus reducing the homogeneous nucleation threshold.

A set of coated and uncoated NP samples with comparable concentrations (*i.e.*, equal absorbance values at 310 nm) were prepared, and their PL was recorded for fresh samples and after four days (storage RH 60%) to evaluate structural stability. The PL spectra and pictures of the samples under UV-light are presented in Fig. 3. Remarkably, PL intensity diminished faster over time in the uncoated NPs. CsPb(Cl$_x$Br$_{3-x}$) NCs suffered a decay of 75%, and the emission peak is blue-shifted from 488 to 458 nm after four days. It could be associated with a reduction in the amount of Br in CsPbX$_3$ that blue-shifts the emission peak. In the case of CsPb(Cl$_x$Br$_{3-x}$)@SiO$_2$ NPs, it barely moved 7 nm and boosted its PL intensity up to 60%; this increase in emission yields over time could be attributed to halide diffusion and rearrangement on nanoparticles con-
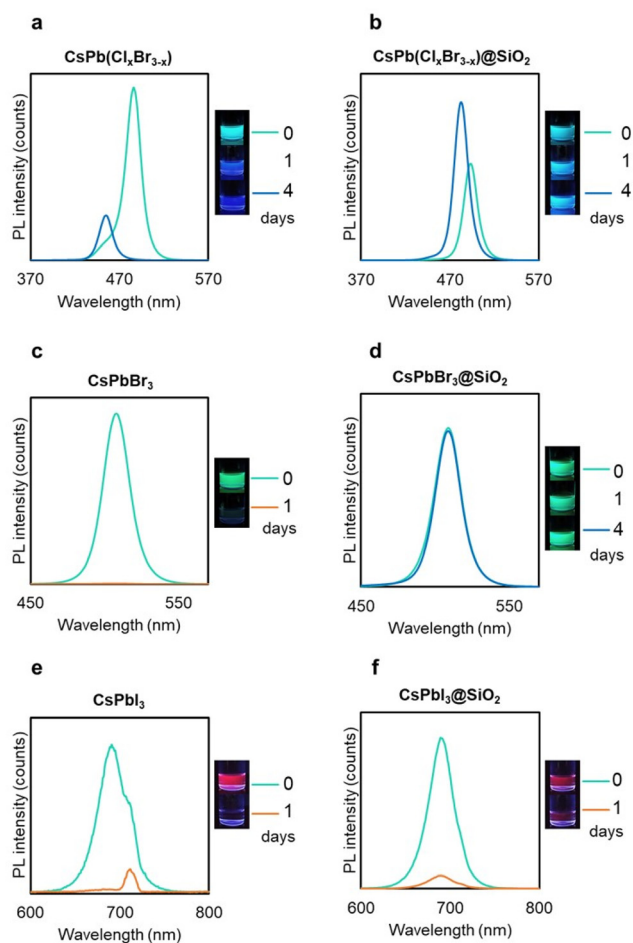
Fig. 3 Emission spectra recorded at an excitation wavelength of 355 nm for fresh (orange) and samples stored at RH 60% (blue) of non-encapsulated $CsPbX_3$ NCs (a, c and e) and $CsPbX_3@SiO_2$ NPs (b, d, and f) prepared at equal concentrations.

fined in the perovskite NCs, reducing nonradiative losses. The photoluminescence of $CsPbBr_3$ NCs was quenched after one day, while $CsPbBr_3@SiO_2$ maintained strong green emission after four days. These results indicate that the SiO_2 coating conferred structural stability at a certain degree against moisture, except for the iodine samples, which both quickly suffered from degradation. The latter could be attributed to the iodine-based perovskites' poor phase and chemical stability, making it difficult to obtain stable NCs in the red region, also called the "perovskite red wall".[38]

Finally, despite the structural stability conferred by the SiO_2 shell coating, it could not withstand the diffusion of water molecules. Consequently, the developed core–shell NPs suffered fast degradation in water. Intending to obtain water-resistant NPs, we performed a straightforward approach based on strategic silica pore collapse under thermal treatment.[39] For this purpose, the core–shell NPs were thermally treated at 565 °C. Under these conditions, the pores of the silica shell transformed into a compact network. In parallel, the subli-mated perovskite NCs were retained inside the silica structure.

In the cooling down process, $CsPbX_3$ NCs were formed again, conferring bright photoluminescence and complete stability against water media to the resulting nanoparticles.

The thermally treated particles maintained their stability in water for four days (Fig. 4). Elemental EDS analysis of calcined samples is depicted in Fig. S4.† The EDS patterns showed an atomic ratio of O to Si of 2. After extracting the silica contribution from elemental composition analysis we observed that mixed halide $CsPb(Br_{0.7}Cl_{0.3})_3$ contained 70% bromine and 30% chloride. Besides that, elemental atomic ratios of small nanocores $(Cs:Pb:X)$ trapped inside are $(1:0.5:0.5)$ and $(1:1.1:0.3)$ for $CsPbBr_3$ and $CsPb(Br_{0.7}Cl_{0.3})_3$, respectively. The deviation from stoichiometry can be attributed to the poor reliability on EDS quantification when the particles are too small and the thickness of the shell is remarkable. According to the literature, our described NPs exhibit more extended stability in pure water solvent (see Table S1 in the ESI†). In this context, it should be stated that conventionally fluorescent probes are presented as lyophilized nanoconjugates in buffer-free media, and immunoassay takes shorter than 1 hour, thus making those NPs suitable for their use as fluorescent probes.

Furthermore, as proof of concept, we tested the as-synthesized NPs as fluorogenic labels for the *in vitro* detection of a humanized antibody (Fig. 5a). For this purpose, the core–shell NPs were conjugated using direct adsorption with omali-zumab (NP-αIgE), a therapeutic antibody used for treating severe asthma. A multi-well black polystyrene plate was coated with a specific receptor for the paratope of the humanized antibody (5 mg L^{-1}). Then, the coated wells were incubated for 1 h at 25 °C with the fluorogenic conjugate, which selectively recognized the receptor. Finally, the photoluminescence spectra were recorded using the EnSpire multimode plate reader (PerkinElmer). As a negative control, wells were coated with ovalbumin protein at 5 mg L^{-1} (for further experimental details, see the Experimental section).
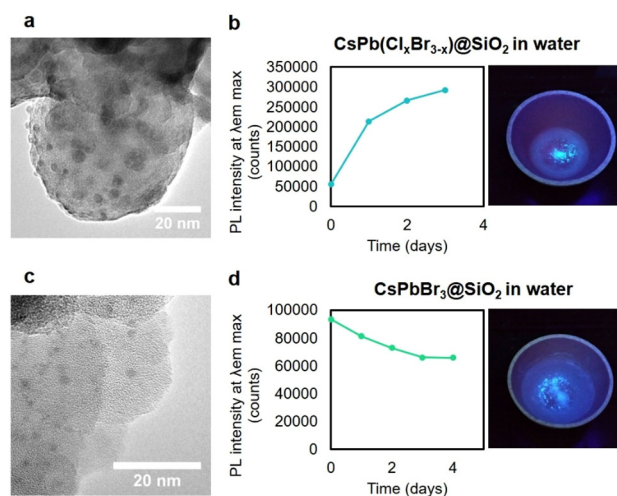

Fig. 4 TEM images of the calcined (a) $CsPb(Cl_x/Br_{3-x})@SiO_2$ and (c) $CsPbBr_3@SiO_2$ NPs and PL intensity at maximum emission *versus* time in water (b and d).
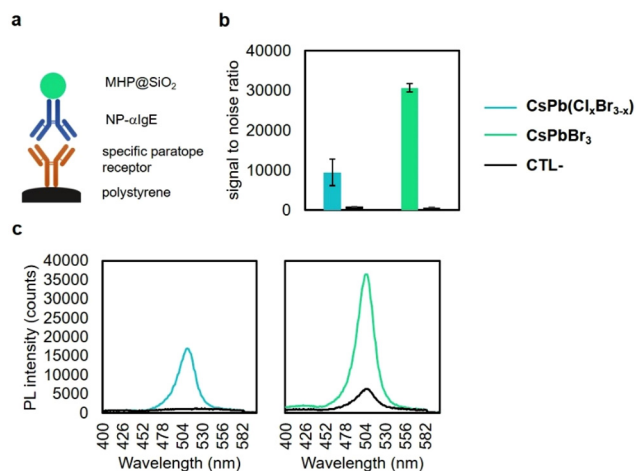
Fig. 5 (a) Schematic illustration of the fluorogenic recognition event. (b) Signal to noise ratio, and (c) photoluminescence spectra of the test (colored line) and control assay (black line).

Fig. 5b and c shows the signal-to-noise ratio and photoluminescence spectra for polystyrene wells incubated with NP-αIgE conjugates. Our results confirmed the successful chemical biorecognition of allergen-specific humanized antibodies, achieving a signal-to-noise ratio of ~10 000 and 30 000 for $CsPb(Cl_xBr_{3-x})$ and $CsPbBr_3$, respectively. Besides, the control experiment showed a negligible photoluminescence signal, revealing excellent selectivity of the assay. Remarkably, $CsPb(Cl_xBr_{3-x})$ presented a similar emission wavelength to that of $CsPbBr_3$ (~505 nm). This fact can be attributed to the poor amount of Cl in the hybrid structure after thermal treatment, as shown in Fig. S4.† We are expanding the methodology to other halide compositions to develop multiplexed immunoassays. Hence, the findings presented herein provide initial evidence of the potential of perovskite nanoparticles as a new fluorogenic probe in immunochemistry. These results pave the way for developing immunoassay tests. As for concerns regarding the toxicity associated with the presence of lead in perovskite compositions, it is essential to note that there is a wide range of *in vitro* applications in biosensing (luminescent microarrays, flow cytometry, paper-based immunoassays, *etc.*) and bioimaging (immunostaining, cell histology, *in vitro* cell tracking, *etc.*) where lead toxicity is not a limiting factor. Additionally, it is worth mentioning that while this work serves as a proof of concept for the suitability of these materials as fluorescent labels, ongoing research is actively exploring lead-free perovskite NCs with reduced toxicity. Thus, we anticipate that this methodology can soon be extended to lead-free perovskite NPs.

using alkoxysilane. Our findings indicate that the initial concentration of Cs_4PbX_6 plays a crucial role in achieving a uniform distribution of monodisperse perovskite core–shell NPs and controlling the number of core-free NPs. By optimizing our method, we successfully obtained core–shell nanoparticles with emissions ranging from 480 to 690 nm. These nanoparticles exhibited small particle sizes (20–30 nm), narrow size distribution cores (2–11 nm), and sharp emission peaks (fwhm of 22–33 nm). Moreover, the core–shell nanoparticles demonstrated structural stability and maintained their luminescence properties under RH of 60% for up to four days. Although previous reports described perovskite core–shell NPs obtained using similar methodologies,[25,27] it is important to highlight that our work goes one step ahead and extends this method to other halide compositions, achieving NPs with a color gamut covering most of the visible region. In addition, according to the literature, the size reduction presents a deleterious effect on the PLQY, and $CsPbBr_3$ NPs described in the literature prepared by exploiting transformative features with sizes below 30 nm are poor emitters. Their PLQYs are almost totally quenched upon coating with SiO_2. Conversely, our NPs' present PLQYs of 18% and 57% for $CsPb(Cl_xBr_{3-x})@SiO_2$ and $CsPbBr_3@SiO_2$ *versus* 10% and 43% of the uncoated counterparts, meaning that the coating yields a recovery factor of 80% and 32%. These data point out the dual functionality of the silica shell, which reduces nonradiative losses *via* shallow defect passivation of $CsPbX_3$ NCs and prevents their structural degradation.

Furthermore, this size reduction has significant implications for practical application in biosensing, as their dimensions are comparable to functional biological units (protein, enzymes, and nucleic acids), allowing for a single tag per biomolecule ratio.[6] Additionally, by employing a controlled postsynthetic thermal treatment, we achieved water-resistant NPs through strategic silica pore condensation of the silica shell pores into a compact shell structure. Remarkably, our developed NPs meet the requirements of size, color gamut, and emission yields, along with their mild synthesis conditions, positioning them as promising labels with the potential to outperform organic dyes, fluorescent proteins, and chalcogenide QDs. The water-stable NPs were successfully conjugated with a humanized antibody to evaluate their viability as fluorescent reporters, demonstrating specific recognition of its paratope.

Although further research is required to synthesize water-stable labels of different halide compositions, we believe that MHP NPs will enable the development of sensitive, multicolor, and multiplexed assays, opening exciting possibilities for their applications in life sciences.

4. Conclusions

In summary, we have developed a simple method for synthesizing $CsPbX_3$ core–shell nanoparticles. This novel approach involves the transformation of water-triggered 0D Cs_4PbBr_6 into $CsPbX_3$, followed by encapsulation inside a silica shell

Author contributions

C. C. designed the methodology, performed the experiments, and wrote the original draft. W. T. carried out thermal treatment studies to obtain water-stable nanoparticles. P. Q. C and S. M. designed the immunoassay and provided the

immunoreagents. V. G. P. conceptualized the investigation and co-wrote, reviewed, and edited the manuscript. M. J. B. and A. M. supervised this study and acquired financial support for the project leading to this publication. All the authors proof-read and approved the final manuscript for submission.

Conflicts of interest

There are no conflicts to declare.

Acknowledgements

References

1 B. A. Koscher, J. K. Swabeck, N. D. Bronstein and A. P. Alivisatos, *J. Am. Chem. Soc.*, 2017, **139**, 6566–6569.

2 L. Protesescu, S. Yakunin, M. I. Bodnarchuk, F. Krieg, R. Caputo, C. H. Hendon, R. X. Yang, A. Walsh and M. V. Kovalenko, *Nano Lett.*, 2015, **15**, 3692–3696.

3 A. Swarnkar, R. Chulliyil, V. K. Ravi, M. Irfanullah, A. Chowdhury and A. Nag, *Angew. Chem., Int. Ed.*, 2015, **54**, 15424–15428.

4 J. Shamsi, A. S. Urban, M. Imran, L. De Trizio and L. Manna, *Chem. Rev.*, 2019, **119**, 3296–3348.

5 P. Dobosz, S. Morais, R. Puchades and A. Maquieira, *Biosens. Bioelectron.*, 2015, **69**, 294–300.

6 S. K. Nune, P. Gunda, P. K. Thallapally, Y. Y. Lin, M. Laird Forrest and C. J. Berkland, *Expert Opin. Drug Delivery*, 2009, **6**, 1175–1194.

7 C. Collantes, W. Teixeira, V. González Pedro, M. J. Bañuls and Á. Maquieira, *Appl. Mater. Today*, 2023, **31**, 101775.

8 C. Meng, D. Yang, Y. Wu, X. Zhang, H. Zeng and X. Li, *J. Mater. Chem. C*, 2020, **8**, 17403–17409.

9 Y. Huang, F. Li, L. Qiu, F. Lin, Z. Lai, S. Wang, L. Lin, Y. Zhu, Y. Wang, Y. Jiang and X. Chen, *ACS Appl. Mater. Interfaces*, 2019, **11**, 26384–26391.

10 W. Wang, J. Li, P. Ni, B. Liu, Q. Chen, Y. Lu, H. Wu, B. Cao and Z. Liu, *ES Mater. Manuf.*, 2019, **4**, 66–73.

11 S. Li, D. Lei, W. Ren, X. Guo, S. Wu, Y. Zhu, A. L. Rogach, M. Chhowalla and A. K. Y. Jen, *Nat. Commun.*, 2020, **11**, 1–8.

12 X. Wang, S. Zhuo, J. Fu, X. Li, X. Zhao, H. Jiang, G. Lv, P. Li, J. Li, W. H. Zhang and W. Ma, *ACS Appl. Mater. Interfaces*, 2023, **15**, 20208–20218.

13 Y. Duan, D. Y. Wang and R. D. Costa, *Adv. Funct. Mater.*, 2021, **31**, 2104634.

14 C. Sun, Y. Zhang, C. Ruan, C. Yin, X. Wang, Y. Wang and W. W. Yu, *Adv. Mater.*, 2016, **28**, 10088–10094.

15 H. Zhao, L. Wei, P. Zeng and M. Liu, *J. Mater. Chem. C*, 2019, **7**, 9813–9819.

16 W. Song, Y. Wang, B. Wang, Y. Yao, W. Wang, J. Wu, Q. Shen, W. Luo and Z. Zou, *Nano Res.*, 2020, **13**, 795–801.

17 V. Malgras, S. Tominaka, J. W. Ryan, J. Henzie, T. Takei, K. Ohara and Y. Yamauchi, *J. Am. Chem. Soc.*, 2016, **138**, 13874–13881.

18 D. N. Dirin, L. Protesescu, D. Trummer, I. V. Kochetygov, S. Yakunin, F. Krumeich, N. P. Stadie and M. V. Kovalenko, *Nano Lett.*, 2016, **16**, 5866–5874.

19 Q. A. Akkerman, S. Park, E. Radicchi, F. Nunzi, E. Mosconi, F. De Angelis, R. Brescia, P. Rastogi, M. Prato and L. Manna, *Nano Lett.*, 2017, **17**, 1924–1930.

20 L. Wu, H. Hu, Y. Xu, S. Jiang, M. Chen, Q. Zhong, D. Yang, Q. Liu, Y. Zhao, B. Sun, Q. Zhang and Y. Yin, *Nano Lett.*, 2017, **17**, 5799–5804.

21 F. Palazon, C. Urso, L. De Trizio, Q. Akkerman, S. Marras, F. Locardi, I. Nelli, M. Ferretti, M. Prato and L. Manna, *ACS Energy Lett.*, 2017, **2**, 2445–2448.

22 F. Palazon, G. Almeida, Q. A. Akkerman, L. De Trizio, Z. Dang, M. Prato and L. Manna, *Chem. Mater.*, 2017, **29**, 4167–4171.

23 T. Udayabhaskararao, L. Houben, H. Cohen, M. Menahem, I. Pinkas, L. Avram, T. Wolf, A. Teitelboim, M. Leskes, O. Yaffe, D. Oron and M. Kazes, *Chem. Mater.*, 2018, **30**, 84–93.

24 D. Baranov, G. Caputo, L. Goldoni, Z. Dang, R. Scarfiello, L. De Trizio, A. Portone, F. Fabbri, A. Camposeo, D. Pisignano and L. Manna, *Chem. Sci.*, 2020, **11**, 3986–3995.

25 M. Li, X. Zhang and P. Yang, *Nanoscale*, 2021, **13**, 3860–3867.

26 S. Park, M. N. An, G. Almeida, F. Palazon, D. Spirito, R. Krahne, Z. Dang, L. De Trizio and L. Manna, *Nanoscale*, 2019, **11**, 18739–18745.

27 C. Rossi, R. Scarfiello, R. Brescia, L. Goldoni, G. Caputo, L. Carbone, D. Colombara, L. De Trizio, L. Manna and D. Baranov, *Chem. Mater.*, 2022, **34**, 405–413.

28 X. Zhang, X. Bai, H. Wu, X. Zhang, C. Sun, Y. Zhang, W. ei Zhang, W. Zheng, W. W. Yu, L. Andrey Rogach, D. Zhang, X. Bai, H. Wu, C. Sun, Y. Zhang, W. W. Yu, W. Zhang, W. Zheng and A. L. Rogach, *Angew. Chem., Int. Ed.*, 2018, **57**, 3337–3342.

29 Q. Zhong, M. Cao, H. Hu, D. Yang, M. Chen, P. Li, L. Wu and Q. Zhang, *ACS Nano*, 2018, **12**, 8579–8587.

30 F. Gao, W. Yang, X. Liu, Y. Li, W. Liu, H. Xu and Y. Liu, *Chem. Eng. J.*, 2021, **407**, 128001.

31 M. R. Kar, R. Chakraborty, U. Patel, S. Ray, T. K. Acharya, C. Goswami and S. Bhaumik, *Mater. Today Chem.*, 2022, **23**, 100753.

32 H. Hu, L. Wu, Y. Tan, Q. Zhong, M. Chen, Y. Qiu, D. Yang, B. Sun, Q. Zhang and Y. Yin, *J. Am. Chem. Soc.*, 2018, **140**, 406–412.

33 C. Zheng and O. Rubel, *J. Phys. Chem. C*, 2019, **123**, 19385–19394.

34 J. H. Noh, S. H. Im, J. H. Heo, T. N. Mandal and S. Il Seok, *Nano Lett.*, 2013, **13**, 1764–1769.

35 V. K. Lamer and R. H. Dinegar, *J. Am. Chem. Soc.*, 1950, **72**, 4847–4854.

36 H. L. Ding, Y. X. Zhang, S. Wang, J. M. Xu, S. C. Xu and G. H. Li, *Chem. Mater.*, 2012, **24**, 4572–4580.

37 C. Collantes, V. González Pedro, M.-J. Bañuls and Á. Maquieira, *ACS Appl. Nano Mater.*, 2021, **4**, 2011–2018.

38 L. Protesescu, S. Yakunin, S. Kumar, J. Bär, F. Bertolotti, N. Masciocchi, A. Guagliardi, M. Grotevent, I. Shorubalko, M. I. Bodnarchuk, C. J. Shih and M. V. Kovalenko, *ACS Nano*, 2017, **11**, 3119–3134.

39 Q. Zhang, B. Wang, W. Zheng, L. Kong, Q. Wan, C. Zhang, Z. Li, X. Cao, M. Liu and L. Li, *Nat. Commun.*, 2020, **11**, 1–9.